Modeling the fractal geometry of Arctic melt ponds using the level sets of random surfaces

Brady Bowen, Courtenay Strong, and Kenneth M. Golden

Abstract. During the late spring, most of the Arctic Ocean is covered by sea ice with a layer of snow on top. As the snow and sea ice begin to melt, water collects on the surface to form melt ponds. As melting progresses, sparse, disconnected ponds coalesce to form complex, self-similar structures which are connected over large length scales. The boundaries of the ponds undergo a transition in fractal dimension from 1 to about 2 around a critical length scale of 100 square meters, as found previously from area–perimeter data. Melt pond geometry depends strongly on sea ice and snow topography. Here we construct a rather simple model of melt pond boundaries as the intersection of a horizontal plane, representing the water level, with a random surface representing the topography. We show that an autoregressive class of anisotropic random Fourier surfaces provides topographies that yield the observed fractal dimension transition, with the ponds evolving and growing as the plane rises. The results are compared with a partial differential equation model of melt pond evolution that includes much of the physics of the system. Properties of the shift in fractal dimension, such as its amplitude, phase and rate, are shown to depend on the surface anisotropy and autocorrelation length scales in the models. Melting-driven differences between the two models are highlighted.

Mathematics Subject Classification (2010). 51, 35, 42, 86.

Keywords. Fractal geometry, sea ice, Arctic melt ponds, Fourier series, random surfaces, level sets.

1. Introduction

Polar sunrise leads to the melting of snow on the surface of sea ice in the frozen Arctic Ocean. The melt water collects in surface pools called *melt ponds*. While white snow and ice reflect the majority of incident sunlight, melt ponds absorb most of it. The albedo of sea ice floes, which is the ratio of reflected sunlight to incident sunlight, is determined in late spring and summer primarily by the evolution of melt pond geometry [23, 20]. The overall albedo of the sea ice

pack itself then depends on the configurations of ice floes and ponds, as well as the area fraction of open ocean [28]. As melting increases, the albedo of the ice pack decreases, thus leading to more solar absorption and more melting, further decreasing the albedo, and so on. This *ice–albedo feedback* has played a significant role in the rapid decline of the summer Arctic ice pack [19], which most climate models underestimated [24, 2]. Sea ice albedo has been a significant source of uncertainty in climate projections and remains a fundamental challenge in climate modeling [6, 23, 15, 20]. Overall, even in the simplest energy balance models used to predict Earth's equilibrium temperature [12], the albedo is the most important parameter except for the amount of solar energy incident on Earth.

From the first appearance of visible pools of water, often in early June, the area fraction of sea ice covered by melt ponds can increase rapidly to over 70% in just a few days [20, 22], dramatically lowering the albedo. The resulting increase in solar absorption in the surrounding ice and upper ocean further accelerates melting [17], possibly triggering ice-albedo feedback. The spatial coverage and distribution of melt ponds on the surface of ice floes and the open water between the floes thus exert primary control on ice pack albedo and the budget of solar energy in the ice-ocean system [4, 20]. Some images of melt ponds illustrating the evolution of pond connectivity are shown in Figure 1.
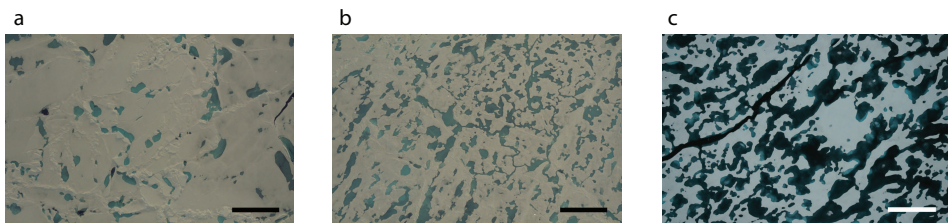

Figure 1. Examples of melt ponds on summer Arctic sea ice. The aerial photos in (a) and (b) were taken in early July during the 1998 Surface Heat Budget of the Arctic Ocean (SHEBA) Experiment [18], and the photo in (c) was taken in late August during the 2005 Healy–Oden TRans Arctic EXpedition (HOTRAX) [16]. The images depict the evolution of melt pond connectivity, with disconnected ponds in (a), transitional ponds in (b), and fully connected melt ponds in (c). The scale bars represent 200 m for (a) and (b), and 35 m for (c).

While melt ponds form a key, iconic component of the Arctic marine environment, comprehensive observations or theories of their formation, coverage, and evolution remain sparse. Available observations of melt ponds show that their areal coverage is highly variable, particularly for first year ice early in the melt season, with rates of change as high as 35% per day [22, 20]. This variability, coupled with the influence of many competing factors controlling melt pond and ice floe

evolution, makes the incorporation of realistic treatments of albedo into climate models quite difficult [20]. Small and medium scale models of melt ponds that include some of these mechanisms have been developed [5, 25, 23], and melt pond parameterizations are being incorporated into global climate models [6, 10, 15].

Analysis of area–perimeter data from hundreds of thousands of melt ponds revealed an unexpected separation of scales, where the pond fractal dimension D, calculated using area–perimeter methods, exhibits a transition from 1 to about 2, around a critical length scale of 100 square meters in area [9], as shown in Figure 2. Pond complexity increases rapidly through the transition region and reaches a maximum for ponds larger than $1000\,\text{m}^2$ whose boundaries resemble space filling curves [21] with $D \approx 2$. This change in fractal dimension is important for the evolution of melt ponds in part because it regulates the extent of the water-ice interface where lateral expansion of the ponds can occur. In fact, the existence of multiple equilibria in a simple energy balance model has been explored in connection with the transition in fractal dimension displayed by Arctic melt ponds. Pond area, and thus pond contribution to albedo, scales differently with system size below and above the critical transition length, leading to complex dynamical behavior [27]. Increasing pond fractal dimension may also slow pond deepening, which is important because deeper ponds absorb more solar energy. Moreover, the transition in fractal dimension provides a benchmark result that may be helpful in providing additional observational data for comparison with melt pond parameterizations being incorporated into climate models [6, 10, 15].

Melt pond geometry depends strongly on sea ice and snow topography, and here we investigate an autoregressive class of anisotropic random Fourier surfaces that provide realistic topographies. They yield the observed fractal dimension transition when paired with two simple melt pond models. The first model represents the melt pond surface as a plane rising through the topography, and the second alters the topography via melting and uses partial differential equations to simulate horizontal transport.

The level set model that we develop here for Arctic melt ponds is based on a continuum percolation model which has been used in studies of statistical topographies arising in problems of electronic transport in disordered media and diffusion in plasmas [11]. Percolation analysis of statistical topographies has also been useful in understanding recent observations about ponds in tidal flats [3]. We believe that this type of level set model could potentially be quite useful in climate modeling, as it captures much of the basic behavior of melt ponds, while being computationally much simpler than PDE models incorporating most of the physics of melt pond evolution.
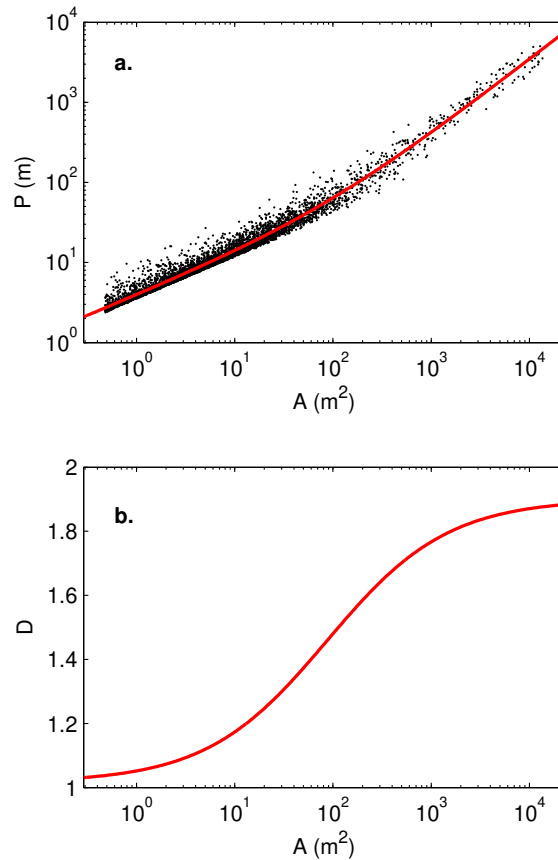
Figure 2. Using the data from [9] shown in (a), the fractal dimension transition can be calculated by taking the derivative of the best fit curve and multiplying by 2, as shown in (b).

The generation of the surfaces that we use as the underlying topography for these models is based on two-dimensional (2D) random Fourier series as detailed in Section 3. Using random Fourier series as our underlying surface generator enables us to generate many surfaces that have certain statistical properties such as anisotropy or autocorrelation length scales. In Section 4, we show that both the plane model and the PDE model provide a sufficiently realistic basis for studying the observed melt pond fractal dimension shift, and there are some interesting contrasts arising from melt-driven modification of the topography in the PDE model. For example, we found that the ability for the PDE model to change its topography significantly increased the depth of its ponds, typically resulting in the PDE model having a greater final fractal dimension than the plane model while also transitioning to this fractal dimension sooner than the plane model.

2. Models

2.1. Evaluating fractal dimension. The main definition of fractal dimension that will be used here [8] involves the following relationship between the areas and perimeters of the ponds,

$$P = kA^{D/2}, \tag{1}$$

where P and A are perimeter and area, respectively, k is a scaling constant, and D is the fractal dimension of the pond boundary. This area-perimeter method for calculating fractal dimension has been used in the sciences for finding the fractal dimension of boundaries when the shapes in question are statistically similar after scaling [1]. Solving for $\log P$ gives the following equation

$$\log P = \frac{D}{2} \log A + \log k. \tag{2}$$

From equation (2), and with k constant under the assumption that the melt ponds are statistically scale invariant, D can be found as twice the slope of a curve which best captures the relationship between the logarithmic variables $y = \log P$ vs. $x = \log A$,

$$D = 2 \frac{dy}{dx}. \tag{3}$$

To find the fractal dimension D as a function of area A based on a large set of observations, in the context of the transitional behavior observed for melt ponds in [9], here we introduce a method based on a least-squares fit to the function

$$D(x) = a_1 \cdot \tanh[a_2(x - a_3)] + a_4. \tag{4}$$

This model allows us to determine the fractal dimension for any value of the area, and yields the following parameters (Figure 3): $D_\infty = a_4 + a_1$, the limiting fractal dimension as area increases, $D_{-\infty} = a_4 - a_1$, the limiting fractal dimension as area approaches zero, and $C = 10^{a_3}$, the inflection point of the curve in units of area. The term $M = a_1 a_4$ is the value of the slope at this inflection point, and is also the maximal slope of the curve. These parameters together characterize how the melt pond fractal dimension varies with area.

In order to solve for the four variables in (4), we first look at the corresponding model for $y = \log P$, which is the result of using separation of variables on (3), substituting into (4) and integrating both sides,

$$y(x) = \frac{1}{2} \int D(x) \, dx = \frac{a_1}{2a_2} \ln(\cosh(a_2(x - a_3))) + \frac{a_4}{2}x + a_5, \tag{5}$$
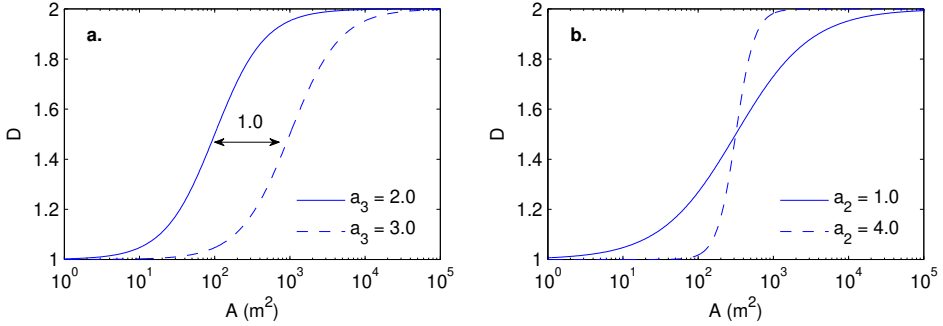
Figure 3. Varying a_3 changes the midpoint as shown in (a), while varying a_2 changes the slope of the function as shown in (b). Similarly, a combination of a_1 and a_4 changes the two asymptotes related to the initial and final fractal dimension.

where a_5 is a constant of integration. Now, equation (5) can be fit to the log A *vs.* log P data by standard methods of nonlinear n-variable regression. This model was used to find the best fit curve and fractal dimension of the melt pond data from [9], as shown in Figure 2.

The fractal dimension calculated using the area-perimeter relation in equation (1) is similar to that calculated through box-counting methods, and they are both asymptotically equivalent to the Hausdorff dimension [8]. Below we will demonstrate the equivalence of box-counting and area-perimeter methods for our pond system by examining the definitions and assumptions made in each case.

Starting from the standard formulation of the box-dimension, let $N(\frac{1}{n})$ be the number of boxes intersecting the perimeter of a pond for a grid with cell dimensions $\frac{1}{n}$ by $\frac{1}{n}$. Then the box-counting dimension D is such that $N(\frac{1}{n}) \approx L_D n^D$ for large n, where L_D is non-zero and finite, and represents the D-dimensional measure of the length of the boundary [8]. We also define $N_2(\frac{1}{n})$ as the number of boxes that intersect the pond including the boundary. Since we assume that the ponds are statistically similar under scaling, as $n \to \infty$ we obtain the following by scaling with a constant c,

$$N\left(\frac{1}{n}\right) \approx c^D N\left(\frac{1}{nc}\right), \tag{6}$$

$$N_2\left(\frac{1}{n}\right) \approx c^2 N_2\left(\frac{1}{nc}\right). \tag{7}$$

Relation (6) comes directly from the definition of the box-dimension, as
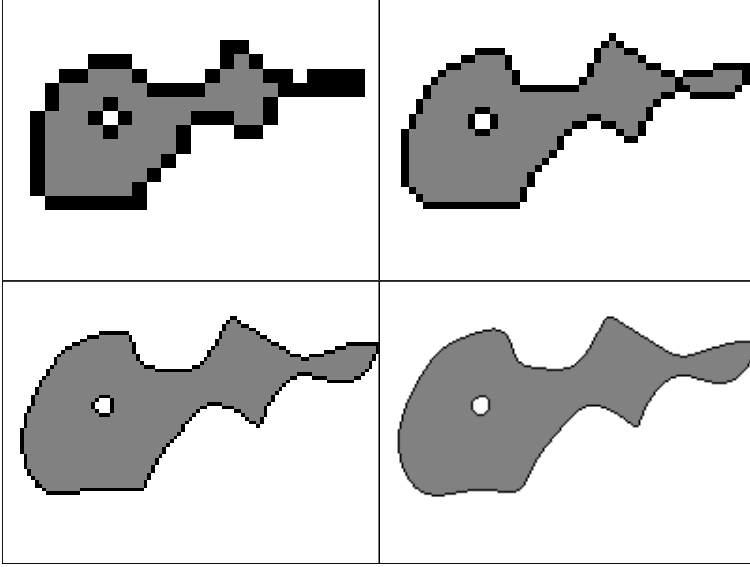
$$N\left(\frac{1}{nc}\right) \approx L_D(nc)^D.$$

Figure 4. Reducing the grid size results in different values for both N and N_2, colored black and gray respectively. Scaling by c has a similar effect on the images. Going left to right, the first row has scaling $c = 1$ and $c = 2$, while the second row has scaling $c = 4$ and $c = 8$.

One may think the same for relation (7), but instead we note that the dimension of area in the plane $\mathbb{R}^2$ is 2. Another motivation for relation (7) comes directly from scaling: as the number of boxes containing the boundary of any pond is negligible compared to the number of boxes inside the pond, we are effectively multiplying the number of boxes inside by c^2 [8]. Solving for c in (7) and substituting it into (6) yields

$$\frac{N\left(\frac{1}{n}\right)}{N\left(\frac{1}{cn}\right)} \approx \left(\frac{N_2\left(\frac{1}{n}\right)}{N_2\left(\frac{1}{cn}\right)}\right)^{D/2}. \tag{8}$$

Since the ponds are statistically similar under scaling by c, then this relation can be re-written as

$$\frac{N\left(\frac{1}{n}\right)}{[N_2\left(\frac{1}{n}\right)]^{D/2}} \approx \frac{N\left(\frac{1}{cn}\right)}{[N_2\left(\frac{1}{cn}\right)]^{D/2}} \approx k, \tag{9}$$

for some constant k. Noting that we can retrieve both perimeter and area from N and N_2, respectively, we obtain the following,

$$N\left(\frac{1}{n}\right) \approx kN_2\left(\frac{1}{n}\right)^{D/2}, \tag{10}$$

or

$$P \approx k A^{D/2}. \tag{11}$$

Therefore, the fractal dimension calculated with box-counting methods is consistent with the fractal dimension retrieved through area-perimeter methods, given the assumption that the ponds are statistically invariant under scaling [8]. To further illustrate the equivalence of the two methods, we consider the Koch curve.
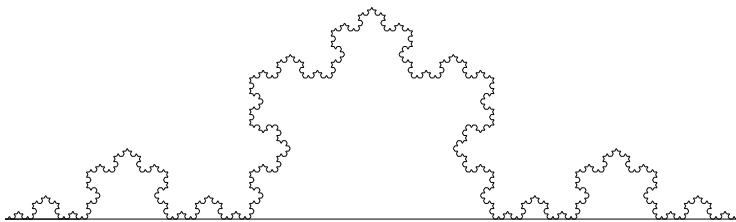

Figure 5. The Koch curve after 6 iterations, along with its base line, to indicate the area contained by the curve.

After a significant number of iterations, the Koch curve becomes self-similar under scaling, yet the perimeter is still finite, allowing us to use the methods above. In this case, scaling two dimensional space by a multiple of $c = 3$ results in the perimeter being scaled by a multiple of 4 and the area being scaled by a multiple of 9. Therefore, when we graph the function representing the curve in the $(\log A, \log P)$-plane and calculate its slope, we get $\frac{\log 4}{\log 9}$. Since the fractal dimension of the curve is equal to twice this value, the resulting fractal dimension of the Koch curve is $D = 2\frac{\log 4}{\log 9} = \frac{\log 4}{\log 3}$, which is consistent with the box-counting calculation of the dimension of the Koch curve [8].

2.2. Melt pond simulation. As noted in the Introduction, we used two models to simulate melt pond evolution using our stochastic surfaces. The first model represents the melt pond surface as a plane rising through the topography represented by the stochastic surface Z, and the second alters the topography via melting and uses partial differential equations to simulate horizontal transport. The meltwater depth h evolves in the PDE model [14] according to the equation

$$\frac{\partial h}{\partial t} = \text{He}(h)\left[-s + \frac{\rho_{\text{ice}}}{\rho_{\text{water}}} m - \nabla \cdot (h\mathbf{u})\right], \tag{12}$$

where the Heaviside step function

$$\text{He}(h) = \begin{cases} 1 & \text{if } h \geq 0, \\ 0 & \text{if } h < 0, \end{cases} \tag{13}$$

prevents h from becoming negative. The parameter $s = 0.8$ cm day^{-1} is the seepage rate, ρ is material density, g is gravitational acceleration, and the ice melt rate m begins at 1.2 cm day^{-1} and increases linearly with melt pond depth up to a maximum of 3.2 cm day^{-1} once the pond is 10 cm or deeper. The horizontal velocity of melt pond water through porous sea ice is governed by Darcy's law

$$\mathbf{u} = -\frac{g\rho_{\text{water}}}{\mu} \Pi_h \nabla \Psi, \tag{14}$$

where $\mu = 1.7 \times 10^{-3}$ kg m^{-1} s^{-1} is the dynamic viscosity, $\Pi_h = 3 \times 10^{-9}$ m^2 is the fluid permeability (taken here to be a constant), and $\Psi = z + h$ is the height of the surface Z at the location plus any overlying melt pond water depth at that location. A detailed discussion of parameter settings and related sensitivity analyses are given in [14].

For the plane model, we define melt ponds as the volume between a plane at elevation $z = z_c$ and the surface topography Z (i.e., a melt pond exists where $Z < z_c$). To correlate the plane model with the PDE model, z_c was chosen at each time step so that the total melt pond water volume was equal over time between the two models. The principal differences between the plane model and PDE model is that the PDE model modifies the topography via melting and simulates horizontal melt water transport, whereas the plane model retains the initial topography through the simulation and assumes instantaneous horizontal transport as the water surface rises.

3. Stochastic surface generation

The surfaces that will be used for studying the two models are generated by a two dimensional Fourier series with random coefficients. In particular, we use a finite cosine expansion with phase given by independent identically distributed (I.I.D.) uniform random variables and amplitude coefficients given by the physical properties of an autoregressive relation. The series that we use has the following form

$$\sum_{n,m=1}^{N} a_{n,m} \cos(mx + ny + \phi_{n,m}), \tag{15}$$
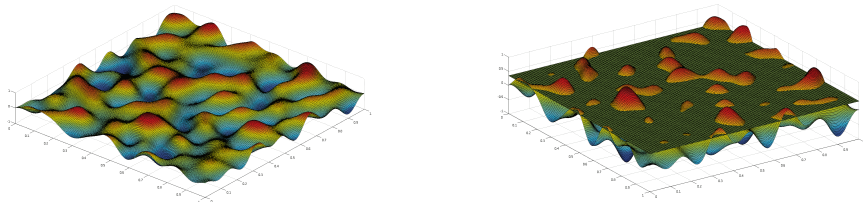
Figure 6. On the left is an example of a surface we use to represent the sea ice topography, and on the right is the intersection of this surface with a plane representing the water level.

where the $a_{n,m}$ are the amplitude coefficients, and the $\phi_{n,m}$ are I.I.D. uniform random variables with values in $[0, 2\pi]$. This formulation enables us to consider random surfaces while still allowing specification of some of the base properties of the surface, namely, the anisotropy and effective range of correlation in each direction. Using Fourier series also allows simplification of the formulas due to the periodicity across the domain.

The intersection of a horizontal plane with a realization of the random surface will represent the boundary of a melt pond in the level set model. Now, since the surface is generated by a finite sum of cosine terms, it is infinitely differentiable, as are the curves defined by the intersection of the surface with the plane. It is reasonable then to ask how we are investigating the fractal dimension of curves in the plane with such a model, particularly when many famous examples such as Brownian motion and the Koch, Peano-Hilbert, and Sierpiński curves are nowhere differentiable. The usual constructions of these curves involve starting on a unit scale and then ramifying basic structures in a self-similar fashion on smaller and smaller scales. However, the fractal dimension of such objects can instead be analyzed by starting on a unit scale and then building in a self-similar fashion on larger and larger scales. By smoothing corners one can construct infinitely differentiable, infinitely large versions of these fractal structures with the same fractal dimension. Similarly, in standard lattice percolation models the smallest scale is the unit lattice spacing, and then the fractal and other properties of percolation clusters are studied over large length scales, with a similar situation for some continuum percolation models [11]. This is exactly the type of behavior we observed in [9], where real Arctic melt ponds – on much larger scales – start exhibiting the elements of self-similarity expected of fractals. This large-scale fractal behavior is seen in other examples in nature, such as in the coastline of Britain. In order to capture the *transition* in fractal dimension that we have observed in nature, we use the area-perimeter method described in Section 2.1. Finding classes of surfaces which would ultimately yield the observed patterns and fractal properties of Arctic melt ponds was a challenging problem.

3.1. Autoregressive model. In order to choose the topographic amplitudes, we use an autoregressive relationship. An AR(1) process is defined by the following equation,

$$X_{t+1} = \rho X_t + \epsilon_t, \tag{16}$$

where X_{t+1} and X_t are the values of X at $t+1$ and t, respectively, $\rho \in (-1, 1)$ is the AR(1) coefficient and ϵ_t is white noise with variance σ^2. This AR(1) process has the spectrum [7]

$$\mathcal{S} = \frac{\sigma^2}{1 - 2\rho \cos(f) + \rho^2}, \tag{17}$$

where $f \in [0, 1]$ is the frequency normalized by its maximum value. Further, the integral of $\mathcal{S}$ over all values of f gives the following relation [7],

$$\int_0^1 \mathcal{S} df = \int_0^1 \frac{\sigma^2}{1 - 2\rho \cos(f) + \rho^2} df = 1/(1 - \rho^2).$$

As the surfaces we are looking at involve two independent orthogonal vectors, we want to find a spectrum such that the restriction of the surface to one of these vectors returns an AR(1) process. Let

$$\mathcal{S} = \frac{\sigma^2}{(1 - 2\rho_1 \cos(f_1) + \rho_1{}^2)(1 - 2\rho_2 \cos(f_2) + \rho_2{}^2)} \tag{18}$$

be this spectrum [13].

To show that this spectrum reduces to an AR(1) process along the specified vectors, all that needs to be shown is that the integral over one of the vectors gives an AR(1) process for the other vector. Taking the integral of $\mathcal{S}$ over the values of f_2 yields

$$\int_0^1 \mathcal{S} df_2 = \int_{f_2 \in [0,1]} \frac{\sigma^2}{(1 - 2\rho_1 \cos(f_1) + \rho_1{}^2)(1 - 2\rho_2 \cos(f_2) + \rho_2{}^2)} df_2$$

$$= \frac{\sigma^2}{(1 - 2\rho_1 \cos(f_1) + \rho_1{}^2)} \int_0^1 \frac{1}{(1 - 2\rho_2 \cos(f_2) + \rho_2{}^2)} df_2$$

$$= \frac{\sigma^2}{(1 - 2\rho_1 \cos(f_1) + \rho_1{}^2)} \frac{1}{1 - \rho_2{}^2}.$$

Letting $\sigma'^2 = \frac{\sigma^2}{1 + \rho_2{}^2}$ gives us the required form for an AR(1) process,

$$\int_0^1 \mathcal{S} df_2 = \frac{\sigma'^2}{(1 - 2\rho_1 \cos(f_1) + \rho_1{}^2)}.$$

Therefore, $\mathcal{S}$ is one of these spectra, and is what we will be using for melt pond generation.

3.2. Variogram of 2D Fourier Series. The variogram is a measure of the degree of correlation the value at one point has to the value at another point some "lag" distance away. It will be used to determine the range of each surface, as well as its anisotropy. Typically used in the geosciences, the variogram has the following structure,

$$2\gamma(\mathbf{p}, \mathbf{p} + \mathbf{h}) = \text{Var}(|Z(\mathbf{p}) - Z(\mathbf{p} + \mathbf{h})|), \qquad (19)$$

where $\mathbf{h} = (h_x, h_y)$ is the lag distance vector and Z is the surface to which we are applying a variogram analysis. The vector $\mathbf{p} = (x, y)$ is the set of data points that we are using to calculate the variance of the surface. In order to determine the properties of the variogram when applied to a Fourier series, we use the following notation to describe the variogram of a surface Z,

$$2\gamma_Z(\mathbf{h}) = 2\gamma(\mathbf{p}, \mathbf{p} + \mathbf{h}) = \text{Var}(Z(\mathbf{p}) - Z(\mathbf{p} + \mathbf{h})). \qquad (20)$$

Theorem 1. *Given a surface $Z = a\cos(mx + ny + \theta)$, the variogram of Z over $x, y \in [0, 2\pi]$ is*

$$2\gamma_Z(\boldsymbol{h}) = 2a^2 \sin^2\left(\frac{mh_x + nh_y}{2}\right). \qquad (21)$$

Proof. In order to calculate the variance represented in equation (20) we need to randomly sample the vector $\mathbf{p}$ over the domain $[0, 2\pi] \times [0, 2\pi]$. Let $X = \text{unif}(0, 2\pi)$ and $Y = \text{unif}(0, 2\pi)$ be the uniform random variables sampling $\mathbf{p} = (x, y)$. Then Z can be represented as $Z = a\cos(mX + nY + \theta)$. From this we will directly calculate the variogram of Z,

$$2\gamma_Z(\mathbf{h}) = \text{Var}(a\cos(mX + nY + \theta) - a\cos(m(X + h_x) + n(Y + h_y) + \theta))$$

$$= \text{Var}\left(-2a\sin\left(\frac{(mX + nY + \theta) + (m(X + h_x) + n(Y + h_y) + \theta)}{2}\right)\right.$$
$$\left.\sin\left(\frac{-mh_x - nh_y}{2}\right)\right)$$

$$= 4a^2 \sin^2\left(\frac{mh_x + nh_y}{2}\right)\text{Var}\left(\sin\left(\frac{2mX + 2nY + 2\theta + mh_x + nh_y}{2}\right)\right).$$

This should be equal to $2a^2 \sin^2\left(\frac{mh_x + nh_y}{2}\right)$ if the remaining variance is equal to 1/2. In order to show this, we first use the following substitutions and calculations,

$$X_1 = \cos\left(\frac{2mX + mh_x + \theta}{2}\right), \qquad E(X_1^2) = \frac{1}{2}, \qquad E(X_1)^2 = 0,$$

$$X_2 = \sin\left(\frac{2mX + mh_x + \theta}{2}\right), \qquad E(X_2^2) = \frac{1}{2}, \qquad E(X_2)^2 = 0,$$

$$Y_1 = \cos\left(\frac{2nY + nh_y + \theta}{2}\right), \qquad E(Y_1^2) = \frac{1}{2}, \qquad E(Y_1)^2 = 0,$$

$$Y_2 = \sin\left(\frac{2nY + nh_y + \theta}{2}\right), \qquad E(Y_2^2) = \frac{1}{2}, \qquad E(Y_2)^2 = 0.$$

From here, we can use the double angle formula to compute the variance,

$$\operatorname{Var}\left(\sin\left(\frac{2mX + 2nY + 2\theta + mh_x + nh_y}{2}\right)\right)$$

$$= \operatorname{Var}(X_1Y_1 - X_2Y_2)$$

$$= \operatorname{Var}(X_1Y_1) + \operatorname{Var}(X_2Y_2) + \operatorname{Cov}(X_1Y_1, X_2Y_2)$$

$$= E(X_1^2)E(Y_1^2) - E(X_1)^2E(Y_1)^2 + E(X_2^2)E(Y_2^2) - E(X_2)^2E(Y_2)^2 + 0$$

$$= \frac{1}{2}\cdot\frac{1}{2} - 0 + \frac{1}{2}\cdot\frac{1}{2} - 0$$

$$= \frac{1}{2}.$$

Therefore, the value of the remaining variance is $1/2$, as needed. $\square$

Due to the orthogonality properties of cosine, the variogram of a finite Fourier series can be found by computing the sum of the variograms of each element, resulting in the following relations,

$$2\gamma_{aZ}(\mathbf{h}) = 2a^2\gamma_Z(\mathbf{h}), \tag{22}$$

$$2\gamma_{Z+Z'}(\mathbf{h}) = 2\gamma_Z(\mathbf{h}) + 2\gamma_{Z'}(\mathbf{h}). \tag{23}$$

This allows for quick computation of the variogram for each surface, and also shows that the only component that affects the variogram of the surface is the amplitude of the cosine terms. The above proof does not require a specific amplitude distribution, allowing us to compute the variogram for any distribution. As the random phase angle is omitted in the computation of the variogram, generating surfaces that share the same anisotropy and range becomes a trivial matter of using the same amplitudes, and thus spectrum, for both.

3.3. Range and Anisotropy. Now that we can find the variance of any Fourier series, we can use the variogram definition to determine the range and anisotropy for each autoregressive coefficient pair (ρ_1, ρ_2). Therefore, surfaces can be arranged by their anisotropy value $\mathcal{A}$ and the autoregression value of the x-direction as the pair $(\mathcal{A}, \rho)$. This also allows us to choose a length scale representative of Arctic melt pond data.

The use of variograms gives us an effective tool to calculate range between our models and observed data. This range is defined as the distance at which the variogram first achieves 95% of its maximum value. As every random Fourier series with a given autoregressive coefficient pair has the same variogram, we can compute the range for each surface. The definition that we will be using for anisotropy is the ratio $\mathcal{A} = \frac{\text{range}_2}{\text{range}_1}$ where $\text{range}_2 > \text{range}_1$. This definition is primarily used to describe the results and has a positive correlation with other definitions of anisotropy. The following Table 3.3 displays the range for 10 values of ρ, sampled along one of the major axes.

ρ	range	ρ	range
0	0.1458	0.5	0.1885
0.1	0.1532	0.6	0.1972
0.2	0.1613	0.7	0.2047
0.3	0.1701	0.8	0.2106
0.4	0.1793	0.9	0.2141

Given that the range is a fixed value for each choice of ρ, we can use it to define a length scale for each surface. Realistic values of the range were chosen based on values presented in Figure 12 of [26], and our analysis of the snow and ice topography data shown in Figure 11 of the same manuscript. Specifying the range enables us to assign our surfaces a grid spacing in meters. This constant is necessary for the use of the PDE model where we need to know the horizontal grid spacing. While it is less important for the plane model, the length scale is still needed to determine the scale of the fractal dimension transition in meters.

4. Results

4.1. Surface Analysis. The selection of the autocorrelation coefficients drastically affects the shape of the ponds as well as their overall structure and mean direction. Using equation (4) to analyze the melt ponds from both the PDE and the plane model, we found that there was a fractal dimension shift regardless of the values of the auto-correlation coefficients (e.g., Figure 7).

As seen in Figure 8, higher values of anisotropy resulted in pond elongation along the x-axis, and higher values of the auto-correlation [AR(1)] coefficient ρ resulted in larger scale features. To compare and contrast the fractal dimension change between the two melt pond models, we use the same axes of anisotropy and AR(1) coefficient ρ in Figure 9a-f.

There are several general features apparent in both models. The limiting maximum fractal dimension (Figure 9a,d) tends to primarily increase with decreasing
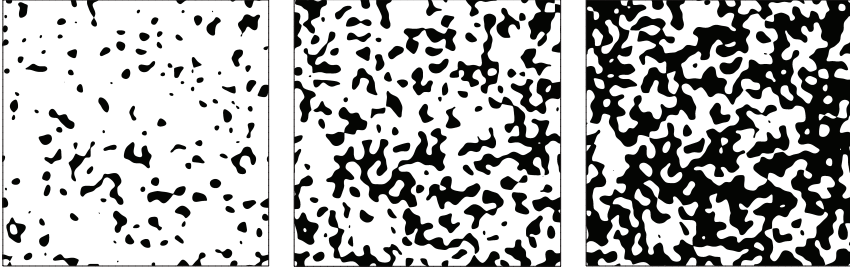
Figure 7. As the plane rises through the generated surface, we see different stages of melt pond growth. When the plane is at 30% (left image) of the maximum height, the melt ponds are just starting to form, with simple, disconnected shapes. At 40% (center image), the melt ponds have become more complex, joining up so that proto-fractal boundaries form between black and white. Most of the individual melt ponds have coalesced at 47.5% (right image) into one giant, complex melt pond with a fractal boundary.

ρ, especially in the PDE model. The anisotropy, by contrast, has minimal influence on the limiting fractal dimension. While the PDE model reaches a maximum fractal dimension of approximately 1.8, the plane model only reaches 1.7. Similarly, the minimum of the PDE model is around 1.55 at the extremum of the values while the plane model can have a minimum limiting fractal dimension of 1.35. Looking at how the initial surfaces were generated, this change in the maximum fractal dimension makes physical sense. When the Fourier series is primarily populated by high frequency waves there is a greater chance of interference between the waves. It is this interference that causes the small channels and lengthy perimeters that result in higher maximum fractal dimension. A similar statement can be made about the Fourier series dominated by low frequency waves. As there is less extreme interference, the ponds tend to be compact with the only sign of interference being the curved boundaries.

Another important relation between the models is the initial fractal dimension (Figure 9c,f). While the noise in the PDE model data can be attributed to the volatility of the random Fourier series, the plane model helps show the main trend that the maximum initial fractal dimension occurs at the upper boundary of anisotropy, and in general a decrease in anisotropy or an increase in ρ decreases this initial dimension down to a limiting value of around 1.15. Our fit to observations in Figure 2 yields a limiting fractal dimension of 1.02, which is close to unity as expected for simple 2D shapes. The inflated value derived from our simulated surfaces likely stems, at least in part, from the grid cells in our simulation domain being approximately 50% larger than those in the melt pond imagery. In other words, recovering the expected slope of unity may require resolving extremely small incipient ponds.
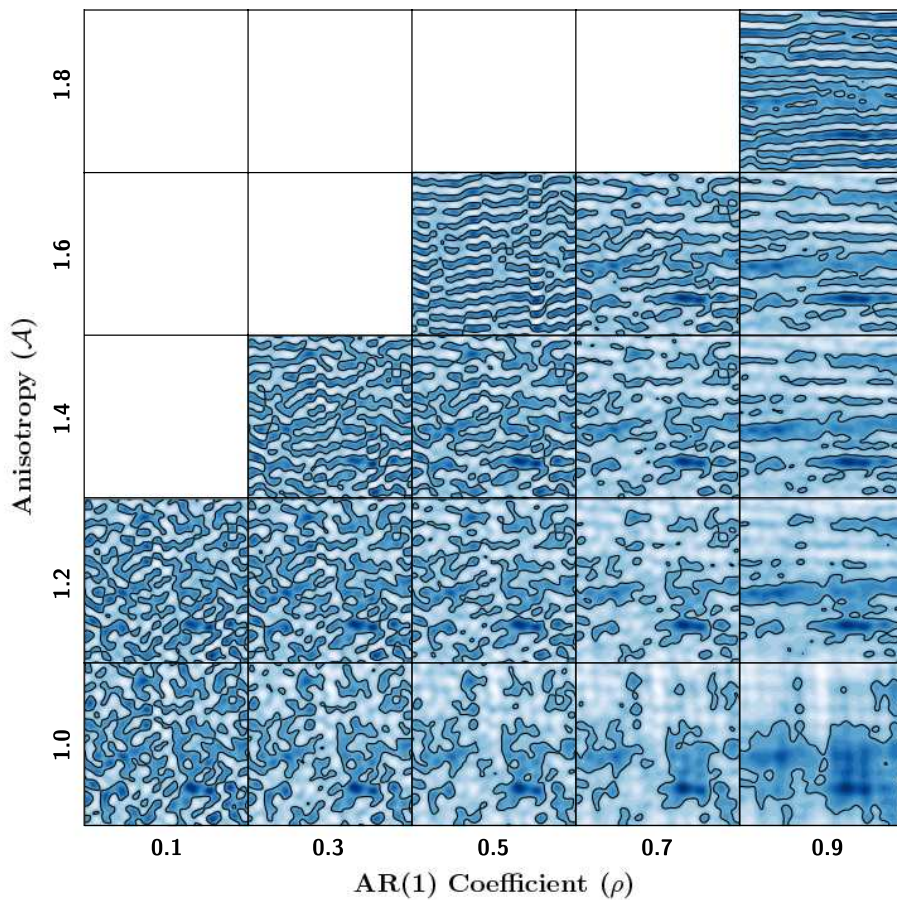
Figure 8. Pond structures generated as a function of anisotropy and ρ in the plane model are shown. Notice that the ponds become more elongated as anisotropy increases while increasing ρ gives rise to more complex pond shapes.
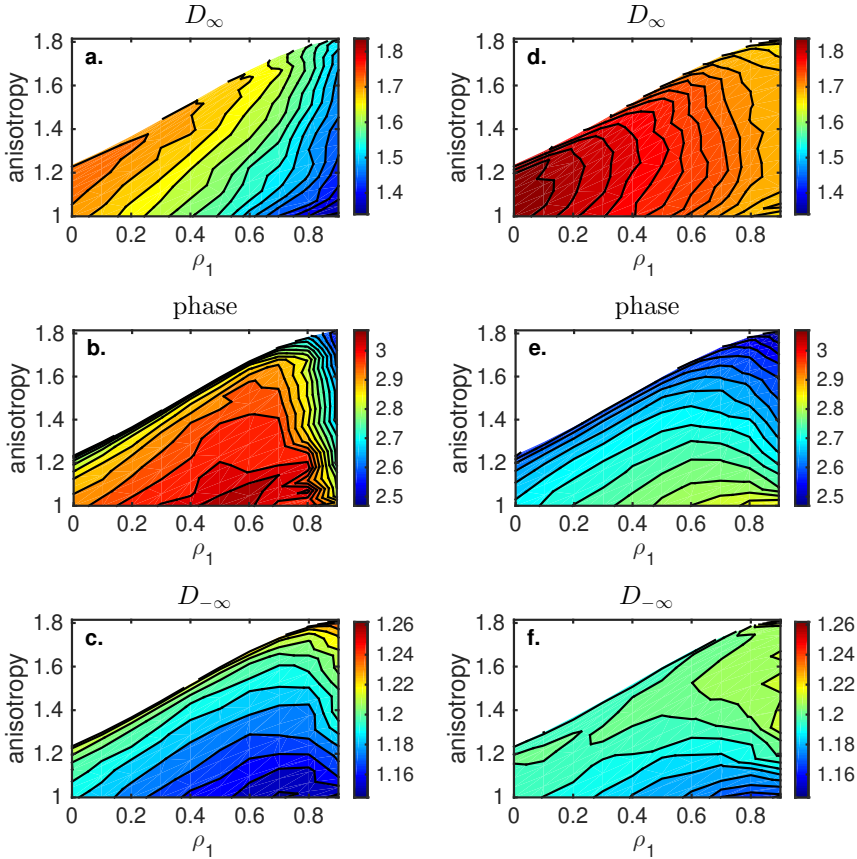
Figure 9. For the plane model, various properties of the fractal dimension shift are shown as a function of anisotropy (A) and autocorrelation in the x-direction (ρ; defined in Section 3.3): (a) D_∞ is the limiting fractal dimension as A increases, (b) phase is the value of $\log(A)$ at which the transition in fractal dimension occurs (a_3 in equation (3)), and (c) $D_{-\infty}$ is the limiting fractal dimension as A decreases to 0 (limit as $\log(A)$ goes to $-\infty$). In (d-f), the same quantities corresponding to (a-c) are shown for the PDE model.

The last major relationship and distinction that we found between the two models was the phase at which the shift in fractal dimension occurred (Figure 9 b,e), where larger phase corresponds to larger total pond area (e.g., Figure 3), as would be seen later in the melt season. We observed that anisotropy strongly influenced the phase of the fractal dimension change. However, in the majority of cases, the plane model transitioned at a later time, roughly an order of magnitude greater than the PDE model.

4.2. Physical Analysis. In order to further analyze the differences between the models, it is useful to compare the evolution of their ponds over time. Figures 10 and 11 show a few time steps for each model on the same surface.
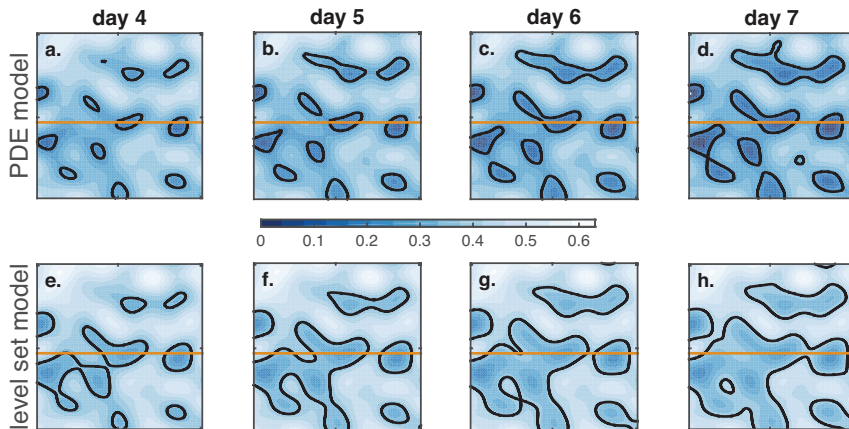

Figure 10. The images show a zoomed-in portion of ponds generated by the PDE and level set models to illustrate their differences. It can be seen that the PDE model better preserves the chaotic boundary while the plane model floods it.

The two main differences between the models are how they deal with where the water accumulates and how their evolution affects the topography of the surface. The PDE model will nearly always immediately fill the local minima of the surface while the plane model instead floods the lowest portions of the surface first. Similarly, the PDE model actively affects the topography, as seen in Figure 11a-d while the plane model does nothing to the topography.

These differences largely explain the contrast between the fractal dimension results of the models. The main reason why the limiting fractal dimension of the plane model is lower than the PDE model on average is due to the plane model flooding the surface, in comparison to the PDE model's tendency to melt downward into the surface and create complex pond shapes (Figure 11). Similarly,
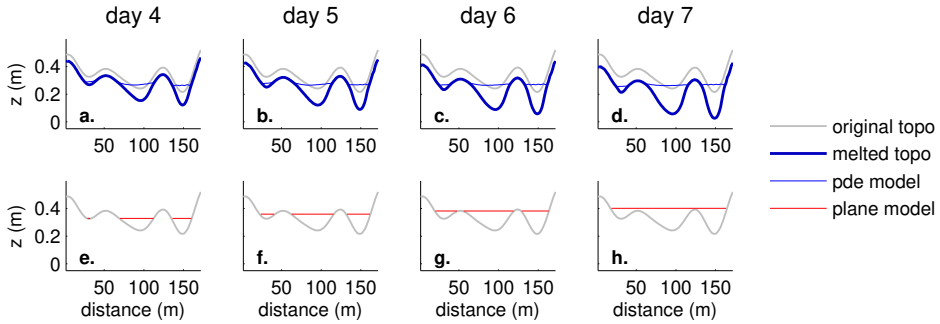
Figure 11. Looking at the height along the yellow line in Figure 10 helps show how the PDE model maintains the fractal boundary while the plane model floods it. In particular, the peak at 50 m is flooded in the plane model while it persists in the PDE model

the size at which these ponds undergo their fractal dimension change is also affected by downward melting. Specifically, the PDE model tends to connect ponds together by thin paths (Figure 10), and these thin paths are usually preserved rather than flooded due to the modification to the topography.

5. Conclusions

In conclusion, we have found a method to generate realistic melt ponds using random Fourier series. These surfaces are constructed using mathematical tools common in statistical physics such as an AR(1) process, which enable us to incorporate some of the properties of actual sea ice topography into the generated models. Therefore, the evolution of the melt ponds produced by these models are realistic in both the length scales and in how fractal dimension evolves with increasing size. Surface anisotropy most heavily influenced the timing (phase) of the fractal dimension transition, whereas surface auto-correlation most heavily influenced the upper limit of pond fractal dimension.

When comparing the plane model to the PDE model, we found some significant differences in the fractal dimension transition between the two. Specifically, the PDE model underwent a later fractal dimension shift (larger phase) and achieved a higher final fractal dimension, in part because of its modification of the topography by melting. Nonetheless, there is enough similarity to consider the plane model as a parsimonious framework that captures first order effects in a computationally efficient and conceptually simple way. Through further modifications to the underlying structure of the random Fourier series, it might be possible to generate melt pond fields that further reflect properties observed in real Arctic melt ponds.

References

[1] P. S. Addison, *Fractals and chaos.* An illustrated course. Institute of Physics Publishing, Bristol, 1997. MR 1483313 Zbl 0888.58027

[2] J. Boé, A. Hall, and X. Qu, September sea-ice cover in the Arctic Ocean projected to vanish by 2100. *Nature Geoscience* **2** (2009), no. 5, 341–343.

[3] B. B. Cael, B. Lambert, and K. Bisson, Pond fractals in a tidal flat. *Phys. Rev. E* **92** (2015), no. 5, 05212.

[4] H. Eicken, T. C. Grenfell, D. K. Perovich, J. A. Richter-Menge, and K. Frey, Hydraulic controls of summer Arctic pack ice albedo. *J. Geophys. Res.* (*Oceans*) **109** (2004), no. C8, C08007.

[5] D. Flocco and D. L. Feltham, A continuum model of melt pond evolution on Arctic sea ice. *J. Geophys. Res.* (*Oceans*) **112** (2007), no. C8, C08016.

[6] D. Flocco, D. L. Feltham, and A. K. Turner, Incorporation of a physically based melt pond scheme into the sea ice component of a climate model. *J. Geophys. Res.* (*Oceans*) **115** (2010), no. C8, C08012.

[7] D. L. Gilman, F. J. Fuglister, and J. M. Mitchell, On the power spectrum of "red noise". *Journal of the Atmospheric Sciences* **20** (1963), no. 2, 182–184.

[8] H. M. Hastings and G. Sugihara, *Fractals.* A user's guide for the natural sciences. Oxford Science Publications. The Clarendon Press, Oxford University Press, New York, 1993. MR 1270447 Zbl 0820.28003

[9] C. Hohenegger, B. Alali, K. R. Steffen, D. K. Perovich, and K. M. Golden, Transition in the fractal geometry of Arctic melt ponds. *The Cryosphere* **6** (2012), no. 5, 1157–1162.

[10] E. C. Hunke and W. H. Lipscomb, CICE: the Los Alamos Sea Ice Model documentation and software user's manual. Version 4.1 LA-CC-06-012, 2010. T-3 Fluid Dynamics Group, Los Alamos National Laboratory.
http://csdms.colorado.edu/w/images/
CICE_documentation_and_software_user's_manual.pdf

[11] M. B. Isichenko, Percolation, statistical topography, and transport in random media. *Rev. Mod. Phys.* **64** (1992), no. 4, 961–1043. MR 1187940

[12] H. Kaper and H. Engler, *Mathematics and climate*. Society for Industrial and Applied Mathematics, Philadelphia, PA, 2013. MR 3137118 Zbl 1285.86001

[13] I. Kennedy, *Transformation of* 1D *and* 2D *autoregressive random fields under coordinate scaling and rotation*. M.A.Sc. Thesis. University of Waterloo, Waterloo, Ontario, Canada, 2008.

[14] M. Lüthje, D. L. Feltham, P. D. Taylor, and M. G. Worster, Modeling the summertime evolution of sea-ice melt ponds. *J. Geophys. Res.* (*Oceans*) **111** (2006), no. C2, C02001.

[15] C. A. Pedersen, E. Roeckner, M. Lüthje, and J. Winther, A new sea ice albedo scheme including melt ponds for ECHAM5 general circulation model. *J. Geophys. Res.* (*Atmospheres*) **114** (2009), no. D8, D08101.

[16] D. K. Perovich, T. C. Grenfell, B. Light, B. C. Elder, J. Harbeck, C. Polashenski, W. B. Tucker III, and C. Stelmach, Transpolar observations of the morphological properties of Arctic sea ice. *J. Geophys. Res.* (*Oceans*) **114** (2009), C00A04.

[17] D. K. Perovich, T. C. Grenfell, J. A. Richter-Menge, B. Light, W. B. Tucker III, and H. Eicken. Thin and thinner: Sea ice mass balance measurements during SHEBA. *J. Geophys. Res.* (*Oceans*) **108** (2003), no. C3, 8050–8071.

[18] D. K. Perovich and W. B. Tucker III and K. A. Ligett, Aerial observations of the evolution of ice surface conditions during summer. *J. Geophys. Res.* (*Oceans*) **107** (2002), no. C10.

[19] D. K. Perovich, J. A. Richter-Menge, K. F. Jones, and B. Light, Sunlight, water, and ice: Extreme Arctic sea ice melt during the summer of 2007. *Geophys. Res. Lett.* **35** (2008), L11501.

[20] C. Polashenski, D. Perovich, and Z. Courville, The mechanisms of sea ice melt pond formation and evolution. *J. Geophys. Res.* (*Oceans*) **117** (2012), no. C1, C01001.

[21] H. Sagan, *Space-filling curves*. Universitext. Springer-Verlag, New York, 1994. MR 1299533 Zbl 0806.01019

[22] R. K. Scharien and J. J. Yackel, Analysis of surface roughness and morphology of first-year sea ice melt ponds: Implications for microwave scattering. *IEEE Trans. Geosci. Rem. Sens.* **43** (2005), no. 12, 2927–2939.eject

[23] F. Scott and D. L. Feltham, A model of the three-dimensional evolution of Arctic melt ponds on first-year and multiyear sea ice. *J. Geophys. Res.* (*Oceans*) **115** (2010), no. C12, C12064.

[24] M. C. Serreze, M. M. Holland, and J. Stroeve, Perspectives on the Arctic's shrinking sea-ice cover. *Science* **315** (2007), 1533–1536.

[25] E. D. Skyllingstad, C. A. Paulson, and D. K. Perovich, Simulation of melt pond evolution on level ice. *J. Geophys. Res.* (*Oceans*) **114** (2009), no. C12, C12019.

[26] M. Sturm, J. Holmgren, and D. K. Perovich, Winter snow cover on the sea ice of the Arctic Ocean at the Surface Heat Budget of the Arctic Ocean (SHEBA): Temporal evolution and spatial variability. *J. Geophys. Res.* (*Oceans*) **107** (2002), no. C10, SHE 23–1–SHE 23–17.

[27] I. A. Sudakov, S. A. Vakulenko, and K. M. Golden, Arctic melt ponds and bifurcations in the climate system. *Commun. Nonlinear Sci. Numer. Simul.* **22** (2015), no. 1-3, 70–81. MR 3282408

[28] T. Toyota, S. Takatsuji, and M. Nakayama, Characteristics of sea ice floe size distribution in the seasonal ice zone. *Geophys. Res. Lett.* **33** (2006), L02616.

Brady Bowen, Department of Mathematics, University of Utah, 155 S 1400 E, RM 233, Salt Lake City, Utah 84112-0090, USA

Current address: Department of Mathematics, Oregon State University, Kidder Hall 368, RM 288, Corvallis, Oregon 97331-4605, USA

e-mail: bradymbowen@gmail.com

Courtenay Strong, Department of Atmospheric Sciences, University of Utah, 135 S 1460 E, RM 819, Salt Lake City, Utah 84112-0110, USA

e-mail: court.strong@utah.edu

Kenneth M. Golden, Department of Mathematics, University of Utah, 155 S 1400 E, RM 233, Salt Lake City, Utah 84112-0090, USA

e-mail: golden@math.utah.edu